applied sciences

MDPI

Article

Impact of Respiratory Gating on Hemodynamic Parameters from 4D Flow MRI

Esteban Denecken [1,2,3,4], Julio Sotelo [1,3,4,5], Cristobal Arrieta [1,3], Marcelo E. Andia [1,3,4,6] and Sergio Uribe [1,3,4,6,*]

1 Biomedical Imaging Center, Pontificia Universidad Católica de Chile, Santiago 782 0436, Chile; ejdenecken@uc.cl (E.D.); julio.sotelo@uv.cl (J.S.); ciarriet@uc.cl (C.A.); meandia@uc.cl (M.E.A.)
2 Department of Electrical Engineering, Pontificia Universidad Católica de Chile, Santiago 782 0436, Chile
3 ANID, Millennium Science Initiative Program, Millennium Nucleus for Cardiovascular Magnetic Resonance, Santiago 782 0436, Chile
4 Instituto Milenio Intelligent Healthcare Engineering, Santiago 782 0436, Chile
5 School of Biomedical Engineering, Universidad de Valparaíso, Valparaiso 236 2905, Chile
6 Department of Radiology, School of Medicine, Pontificia Universidad Católica de Chile, Santiago 832 0000, Chile
* Correspondence: suribe@uc.cl

Abstract: The hemodynamic parameters from 4D flow datasets have shown promising diagnostic value in different cardiovascular pathologies. However, the behavior of these parameters can be affected when the 4D flow data are corrupted by respiratory motion. The purpose of this work was to perform a quantitative comparison between hemodynamic parameters computed from 4D flow cardiac MRI both with and without respiratory self-gating. We considered 4D flow MRI data from 15 healthy volunteers (10 men and 5 women, 30.40 ± 6.23 years of age) that were acquired at 3T. Using a semiautomatic segmentation process of the aorta, we obtained the hemodynamic parameters from the 4D flow MRI, with and without respiratory self-gating. A statistical analysis, using the Wilcoxon signed-rank test and Bland–Altman, was performed to compare the hemodynamic parameters from both acquisitions. We found that the calculations of the hemodynamic parameters from 4D flow data that were acquired without respiratory self-gating showed underestimated values in the aortic arch, and the descending and diaphragmatic aorta. We also found a significant variability of the hemodynamic parameters in the ascending aorta of healthy volunteers when comparing both methods. The 4D flow MRI requires respiratory compensation to provide reliable calculations of hemodynamic parameters.

Keywords: hemodynamics; 4D flow; self-gating; aorta

Citation: Denecken, E.; Sotelo, J.; Arrieta, C.; Andia, M.E.; Uribe, S. Impact of Respiratory Gating on Hemodynamic Parameters from 4D Flow MRI. *Appl. Sci.* **2022**, *12*, 2943. https://doi.org/10.3390/app12062943

Academic Editor: Julio Garcia Flores

Received: 15 December 2021
Accepted: 26 January 2022
Published: 14 March 2022

1. Introduction

Several strategies have been proposed to suppress respiratory motion in cardiac MRI. Most of these techniques are used to track the position of the diaphragm and can be combined with a respiratory-based k-space reordering scheme [1–6]. These techniques include pencil beam navigators [1,2], cross-pair excitation to acquire a column of pixels across the lung-to-liver interface, self-gating strategies based on k_0 points [3], k_0 profiles [4] or 2D image navigators [5].

Newer approaches have achieved respiratory resolved cardiac images with a near 100% respiratory navigator efficiency [7,8]. These approaches have been used to obtain single- or dual-phase 3D whole heart balanced steady state free precession (b-SSFP) images [2], 2D or 3D b-SSFP cine images [9], and 4D flow MRI data [4]. The use of cine b-SSFP respiratory compensated data has remarkably improved the image quality, as well as the anatomical and functional accuracy [7,8]. Nevertheless, there is a debate whether the use of respiratory motion compensation techniques improves the quantification of velocity-derived parameters from the 4D flow MRI [10].

Applying respiratory compensation to 4D flow MRI increases the already long scanning time of this sequence. Moreover, its impact on the accuracy of the hemodynamic parameters remains unclear. Some authors propose that the use of respiratory self-gating techniques has a clear impact on 4D flow measurements by looking at the stroke volume [4,11]. Other studies propose that aorta flow volume quantification does not need respiratory compensation [12]. Other approaches that used profile reordering for respiratory compensation in 4D flow MRI [13,14] suggest that the use of a motion compensation technique increases the accuracy of 4D flow measurements. Most of this discussion has been based on the net flow going through a vessel of interest. However, the net flow is a parameter that averages the velocities in a region of interest, which may hide the distortion of respiratory motion on the velocity field.

Over recent years, several parameters from 4D flow datasets have been derived, such as Wall Shear Stress (WSS), vorticity, helicity, kinetic energy, and viscous dissipation, among others [10,15]. These parameters have been applied in several groups of patients and have shown promising diagnostic value in different cardiovascular pathologies. Nevertheless, these parameters need to be carefully used and compared since their value depends on the resolution and the level of noise of the acquisitions [16]. We also know little about the behavior of these novel parameters when the 4D flow data are corrupted by respiratory motion.

Some of these new hemodynamic parameters are directly proportional to velocity, but others are related to spatial derivatives. Therefore, any rapid perturbation of the velocity field that is introduced by noise or motion could impact the precision and accuracy of the computations. We hypothesized that there are significant differences in the hemodynamic parameters obtained from 4D flow MRI that are acquired with and without respiratory gating in healthy volunteers. The purpose of this work was to perform a quantitative comparison of hemodynamic parameters obtained from 4D flow MRI data that were acquired both with and without respiratory self-gating. We compared the differences between the following hemodynamic parameters, computed in the thoracic aorta: velocity; WSS; WSS axial (WSSA) and circumferential (WSSC) components; vorticity; viscous dissipation; kinetic energy; and energy loss. We also considered the effect of the segmentation process, comparing the segmentations from respiratory self-gated and non-gated data using the DICE as a global index and computing mesh distances to study the local differences.

2. Materials and Methods

2.1. Data Acquisition

This study included thoracic aorta 4D flow MRI data from 15 healthy volunteers (10 men and 5 women, 30.40 $\pm$ 6.23 years of age), which had been previously acquired. The study was conducted according to the guidelines of the Declaration of Helsinki and was approved by the Ethics Committee at Pontificia Universidad Católica (protocol code 171,127,001, 20 June 2019). A 3T Philips MRI scanner was used to acquire the data, with and without respiratory self-gating. The respiratory self-gated strategy consists of the continuous acquisition of the k0 profile and the cross-correlation to determine the respiratory positions [4]. A window of 7 mm was used to collect the data during expiration [4]. A summary of the acquisition parameters is shown in Table 1. The non-respiratory gating scan was acquired with two repetitions (NSA, NEX = 2) in order to have a similar acquisition time to the respiratory self-gated scan.

2.2. Segmentation and Data Processing

Both 4D Flow MRI datasets (with and without respiratory self-gating) were post-processed using an in-house MATLAB toolbox (MathWorks, Natick, MA, USA) [17]. The image processing steps involved the segmentation of the thoracic aorta and the generation of a tetrahedral finite element mesh (characteristic length 1 mm), as described in [18]. The velocity, WSS, WSSA, WSSC, vorticity, viscous dissipation, kinetic energy, and energy loss were obtained from the thoracic aorta 4D flow images, using a least square projection

method based on the finite elements described in [18–20]. All parameters were obtained at a representative peak systolic cardiac phase. These parameters have shown potential value in diagnostics [21]. Angiographic 4D flow images were segmented using a semiautomatic process based on the thresholding, labeling, and manual separation of the vessels. The analysis was performed at the peak systolic phase.

The computations of the hemodynamic parameters were performed using the in-house MATLAB toolbox developed by Sotelo et al. [17] and were exhaustively validated [18–20]. The velocity values were transferred to each node of the mesh from the 3D PC-MRI datasets using a cubic interpolation [18].

Table 1. The MRI acquisition parameters.

Parameter		
Field of view, mm	236 × 226 × 134	
Voxel size, mm	2.34 × 2.34 × 2.5	
Cardiac phases	25	
VENC, cm/s	250	
Echo time, ms	2.66	
Repetition time, ms	4.78–4.80	
Flip angle	5°	
	Self-Gated	Non-Gated
Temporal resolution, ms	37.62 ± 4.43	36.11 ± 4.18
Heart rate, bpm	66.33 ± 7.62	67.93 ± 8.03
Acquisition time, min	15.00 ± 2.86	12.33 ± 0.37

2.3. Statistical Analysis

We assessed the differences between the hemodynamic parameters that were obtained with and without respiratory self-gating over four different regions of the aorta: region I = ascending aorta (between the sinus of Valsalva and before the brachiocephalic trunk); region II = aortic arch (before the brachiocephalic trunk and isthmus level); region III = superior descending aorta (between the isthmus level and the Valsalva level); and region IV = posterior descending aorta (between the Valsalva level and the diaphragmatic aorta). We computed the mean of the measurements in each region to perform the statistical analysis that is presented herein.

Furthermore, we calculated the DICE coefficient between the segmentations of the data that were obtained with and without respiratory self-gating and the local differences between the mesh surfaces of each section. The local differences between both meshes were calculated using the Euclidean distance, as reported in [22].

We analyzed the mean, standard deviation, and coefficient of variation (CV) of each hemodynamic parameter. The Wilcoxon signed-rank test and Bland–Altman plots were also performed between the respiratory self-gated and non-gated data, using a statistical significance of 0.05. We computed the Wilcoxon signed-rank test using the SPSS statistical analysis software and the Bland–Altman plots using MATLAB.

3. Results

Figure 1 shows a representative case of the hemodynamic parameters in the aorta that was obtained from respiratory and non-respiratory gated 4D flow MRI data. By visual inspection, the images look similar. Nevertheless, differences can be observed in the WSS, viscous dissipation, energy loss, and kinetic energy.

Table 2 shows the mean and CV obtained for each hemodynamic parameter at each section of the aorta. The mean of the hemodynamic parameters was similar in section I, but it showed differences in the other sections. Further, the CV values were greater in the 4D flow data acquired without respiratory self-gating compared to the self-gated data. The CV values were greater in section I.

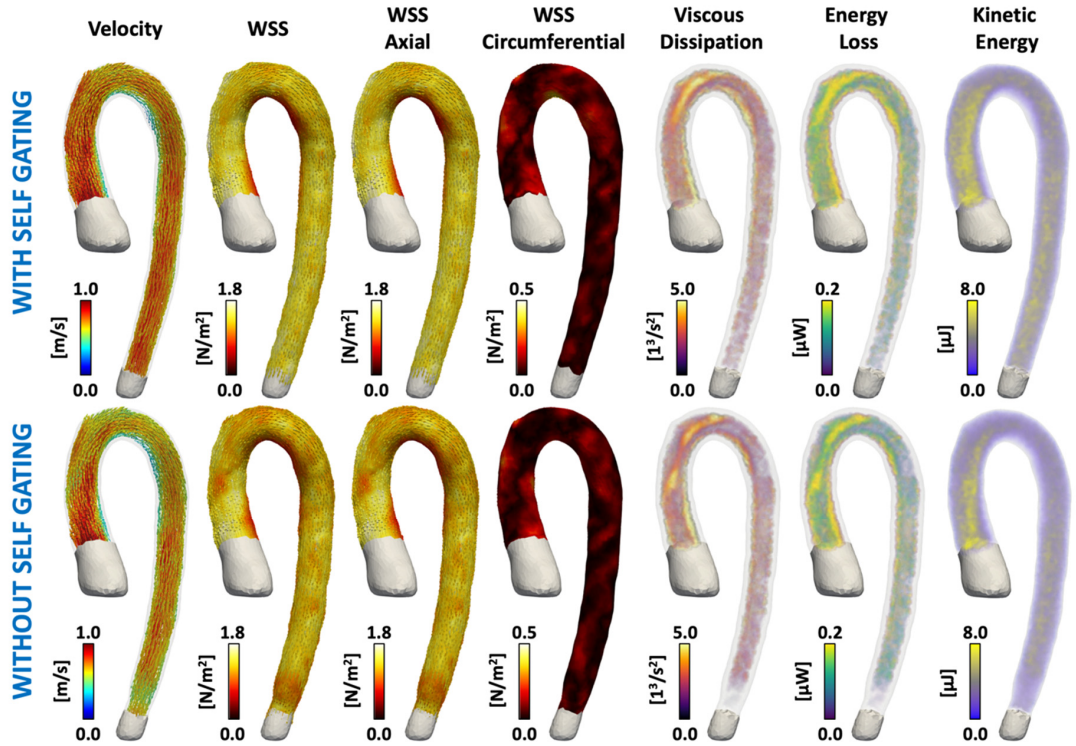

Figure 1. The hemodynamic parameters obtained from 4D flow MRI, both with and without self-gating. In this figure, we show visual representations of the hemodynamic parameters for one volunteer, which were measured at a representative peak systolic cardiac phase.

Table 2. The hemodynamic parameter means and the coefficient of variation (CV) of the mean values at each section of the vessel for the self-gated and non-gated data, which were measured at a representative peak systolic cardiac phase.

	Section I		Section II	
Hemodynamic Parameter	**Self-Gated Mean (CV)**	**Non-Gated Mean (CV)**	**Self-Gated Mean (CV)**	**Non-Gated Mean (CV)**
Velocity (m/s)	0.686 (0.197)	0.652 (0.251)	0.571 (0.159)	0.527 (0.204)
WSS (N/m^2)	1.320 (0.186)	1.265 (0.245)	1.165 (0.138)	1.092 (0.209)
WSSA (N/m^2)	1.308 (0.187)	1.252 (0.242)	1.157 (0.135)	1.084 (0.208)
WSSC (N/m^2)	0.121 (0.343)	0.122 (0.505)	0.101 (0.333)	0.094 (0.302)
Vorticity (1/s)	45.549 (0.310)	45.838 (0.330)	42.008 (0.345)	39.730 (0.370)
Viscous Dissipation ($1/s^2$)	4.569 (0.394)	4.826 (0.590)	3.047 (0.377)	2.611 (0.370)
Kinetic Energy (μJ)	0.258 (0.404)	0.271 (0.601)	0.172 (0.386)	0.147 (0.384)
Energy Loss (μW)	4.303 (0.392)	4.002 (0.479)	2.976 (0.324)	2.572 (0.401)
	Section III		**Section IV**	
Hemodynamic Parameter	**Self-Gated Mean (CV)**	**Non-Gated Mean (CV)**	**Self-Gated Mean (CV)**	**Non-Gated Mean (CV)**
Velocity (m/s)	0.558 (0.205)	0.501 (0.318)	0.528 (0.277)	0.445 (0.375)
WSS (N/m^2)	1.230 (0.198)	1.099 (0.318)	1.224 (0.268)	1.027 (0.384)
WSSA (N/m^2)	1.228 (0.198)	1.096 (0.319)	1.222 (0.268)	1.024 (0.385)
WSSC (N/m^2)	0.048 (0.314)	0.049 (0.316)	0.047 (0.254)	0.051 (0.330)
Vorticity (1/s)	35.541 (0.258)	32.558 (0.306)	41.900 (0.312)	34.369 (0.287)
Viscous Dissipation ($1/s^2$)	1.999 (0.471)	1.753 (0.580)	2.394 (0.643)	1.803 (0.545)
Kinetic Energy (μJ)	0.112 (0.477)	0.097 (0.588)	0.132 (0.637)	0.099 (0.553)
Energy Loss (μW)	2.995 (0.410)	2.523 (0.579)	2.873 (0.510)	2.184 (0.642)

Table 3 shows the results obtained from the statistical analysis. The Wilcoxon signed-rank test showed significant differences between respiratory self-gating and non-respiratory gating in sections II, III, and IV. Differences in velocity, WSS, and WSSA were observed in sections II, III, and IV. There were also statistical differences for viscous dissipation, kinetic energy, and energy loss at sections II and IV.

Table 3. The Wilcoxon signed-rank test *p*-values for the mean values of the hemodynamic parameters at each section of the vessel, between the self-gated and non-gated data.

Hemodynamic Parameter	Section I	Section II	Section III	Section IV
Velocity (m/s)	0.1688	0.0125 *	0.0020 *	0.0003 *
WSS (N/m^2)	0.4212	0.0302 *	0.0015 *	0.0002 *
WSSA (N/m^2)	0.3894	0.0302 *	0.0015 *	0.0002 *
WSSC (N/m^2)	0.4543	0.0946	0.6788	0.3303
Vorticity (1/s)	0.6788	0.1354	0.0833	0.0015 *
Viscous Dissipation ($1/s^2$)	0.6788	0.0215 *	0.0946	0.0302 *
Kinetic Energy (μJ)	0.8904	0.0103 *	0.0554	0.0302 *
Energy Loss (μW)	0.2524	0.0125 *	0.0034 *	0.0003 *

* Existing significative differences.

In Appendix A, Table A1 shows the mean differences and 1.96 times the standard deviation of the Bland–Altman analysis. The 4D flow data with self-gating are used as a reference. The Bland–Altman plots for the velocity and WSS in section I (Figure 2) showed a greater dispersion than sections II, III, and IV. They also show the underestimated values from the data acquired without self-gating. The Bland–Altman plots for velocity, WSS, WSSA, WSSC, vorticity, viscous dissipation, kinetic energy, and energy loss plots are shown in Figure A1. In general, all computations of the hemodynamic parameters acquired without self-gating were underestimated when no respiratory gating was performed. There was a greater difference in velocity, WSS, WSSA, and kinetic energy, and this bias increased along the aortic sections. The standard deviation was greater for most of the parameters in section I compared to other sections.

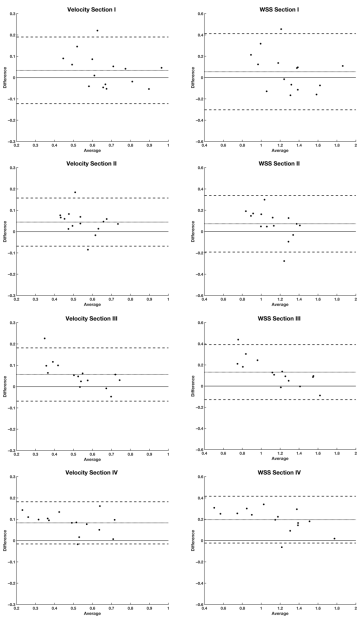

Figure 2. The Bland–Altman plots for velocity and Wall Shear Stress at each section. The difference in Bland–Altman plots was computed as $SG - NG$, where SG is the data with self-gating and NG is the data without self-gating. Appendix A shows the Bland–Altman plots of all hemodynamic parameters considered in this work.

Finally, the mean and range of the DICE coefficient between the segmentation of the self-gated and non-gated data were 0.918 ± 0.056. This result, which considered the whole segmented aorta, showed a high intersection between both segmentations.

A graphical analysis of the local differences [22] between the meshes that were generated from both segmentations shows that the disagreements between them are located at the extremes of the aorta (Figure A2A in Appendix B for one volunteer). The local differences of the segmentations at each section had small variations (Table A2 in Appendix B) and the histogram shows that 88.36% of the differences at each section corresponded to distances lower than or equal to 1 mm (Figure A2B). The local differences were also similarly distributed around the 0% error and thus, there was not a consistent bias between both segmentations.

4. Discussion

In this work, we compared the hemodynamic parameters computed from thoracic aorta 4D flow MRI data that were obtained with and without respiratory self-gating. The statistical descriptors showed that the data obtained with self-gating had less variability than the data obtained without self-gating (Table 2). The Wilcoxon signed-rank test showed significant differences in most of the parameters calculated between both acquisitions at sections II, III, and IV and minimal differences at section I (ascending aorta). Nevertheless, the computations in section I showed a greater variability.

The Bland–Altman analysis showed that the parameters computed without respiratory self-gating were underestimated in comparison to the parameters computed with self-gating and that the underestimation increased along sections II, III, and IV. Section I did not show bias; however, it presented a greater dispersion of the differences for each hemodynamic parameter (see the Bland–Altman plots in Figure A1 in Appendix A). Therefore, for section I, there was not a clear trend of the under- or overestimation of the parameters that were computed. The differences for each volunteer were greater in section I compared to the other sections, which is an important result that is masked by the averaging of all volunteers.

The only parameter that did not show any statistical difference was the WSSC, which is probably due to the near to 0 value of the WSSC in this group of volunteers. An assessment of the impact of respiratory motion on this parameter in a cohort of volunteers or patients with a greater value of WSSC is necessary. As shown by Sotelo et al., there are significant differences in WSSC between healthy volunteers and BAV patients [19].

We also evaluated the impact of the segmentation process as a potential cause of the statistical differences. However, the DICE coefficient and analyses of the local differences at each section showed high agreement between both segmentations and the differences were minimal and unbiased. Therefore, the segmentation did not influence the differences that were observed in the hemodynamic parameters.

A limitation of this study is that we only included healthy volunteers with laminar flow patterns. The next step is to perform a similar study in a group of patients with non-laminar flow patterns or high Reynolds numbers, such as patients with a bicuspid aortic valve (BAV) or with aortic coarctation. Unfortunately, due to the long acquisition time, acquiring two datasets of 4D flow MRI in patients is challenging. Another limitation of the study is that we only assessed the impact of respiratory gating on the hemodynamic parameters at peak systole. The main reason for this was that the poor signal-to-noise ratio of the other cardiac phases makes the segmentation process very challenging. Although it is expected that respiratory motion artifacts may have a stronger effect at lower velocities, this still needs to be proven. Finally, flow parameters as net or regurgitant flow were not included because these results have been presented before using the same datasets [4]. The purpose of this paper was to assess how other hemodynamic parameters are affected by respiratory motion.

In conclusion, we found that the computations of the hemodynamic parameters from 4D flow data using self-gating acquisition showed statistical differences from the

computations from acquisitions without respiratory compensation for the aortic arch and the descending and diaphragmatic aorta in healthy volunteers. The Bland–Altman plots support this fact, showing an underestimation of the hemodynamic parameters acquired without any respiratory compensation. Our results suggest that the use of respiratory motion compensation techniques is mandatory for the accurate evaluation of 4D flow hemodynamic parameters.

Author Contributions: Conceptualization, S.U.; methodology, J.S., M.E.A., S.U. and E.D.; software, J.S.; validation, J.S. and M.E.A.; formal analysis, E.D.; resources, S.U.; data curation, E.D.; writing—original draft preparation, E.D.; writing—review and editing, S.U., J.S. and C.A.; visualization, J.S. and E.D.; supervision, S.U.; project administration, S.U.; funding acquisition, S.U. All authors have read and agreed to the published version of the manuscript.

Funding: This work was funded by ANID—Millennium Science Initiative Program—ICN2021_004, ANID-PIA-ACT192064, ANID—Millennium Science Initiative Program—NCN17_129 and FONDECYT # 1181057. Sotelo J. would like to thank CONICYT-FONDECYT Postdoctorado 2017 #3170737 and FONDECYT de Iniciación en Investigación 2020 #11200481. Andia M. would like to thank FONDECYT # 1180525. Arrieta C. was partially funded by CONICYT FONDECYT Postdoctorado 2019 #3190763, CONICYT PCI REDES 180090, and ANID—Millennium Science Initiative Program—NCN17_129.

Institutional Review Board Statement: The study was conducted according to the guidelines of the Declaration of Helsinki and was approved by the Ethics Committee at Pontificia Universidad Catolica (protocol code 171127001, 20 June 2019).

Informed Consent Statement: Informed consent was not obtained for this study as the data were used retrospectively and obtained in a previous study.

Data Availability Statement: Data are available upon request to the corresponding author.

Conflicts of Interest: The authors declare no conflict of interest.

Appendix A

Bland–Altman Plots

Table A1. The Bland–Altman plots for the mean and standard deviation (Bland–Altman plots show 1.96 × SD).

Hemodynamic Parameter	Section I Mean (SD)	Section II Mean (SD)	Section III Mean (SD)	Section IV Mean (SD)
Velocity (m/s)	0.034 (0.080)	0.045 (0.058)	0.057 (0.064)	0.083 (0.050)
WSS (N/m^2)	0.055 (0.182)	0.074 (0.136)	0.132 (0.132)	0.197 (0.112)
WSSA (N/m^2)	0.056 (0.179)	0.073 (0.135)	0.132 (0.132)	0.197 (0.112)
WSSC (N/m^2)	−0.001 (0.035)	0.007 (0.014)	−0.001 (0.008)	−0.004 (0.014)
Vorticity (1/s)	−0.289 (6.074)	2.279 (8.932)	2.983 (7.033)	7.531 (8.296)
Viscous Dissipation ($1/s^2$)	−0.257 (1.771)	0.436 (0.705)	0.246 (0.587)	0.591 (0.964)
Kinetic Energy (μJ)	−0.013 (0.102)	0.026 (0.040)	0.015 (0.032)	0.032 (0.052)
Energy Loss (μW)	0.301 (0.870)	0.404 (0.581)	0.472 (0.455)	0.689 (0.498)

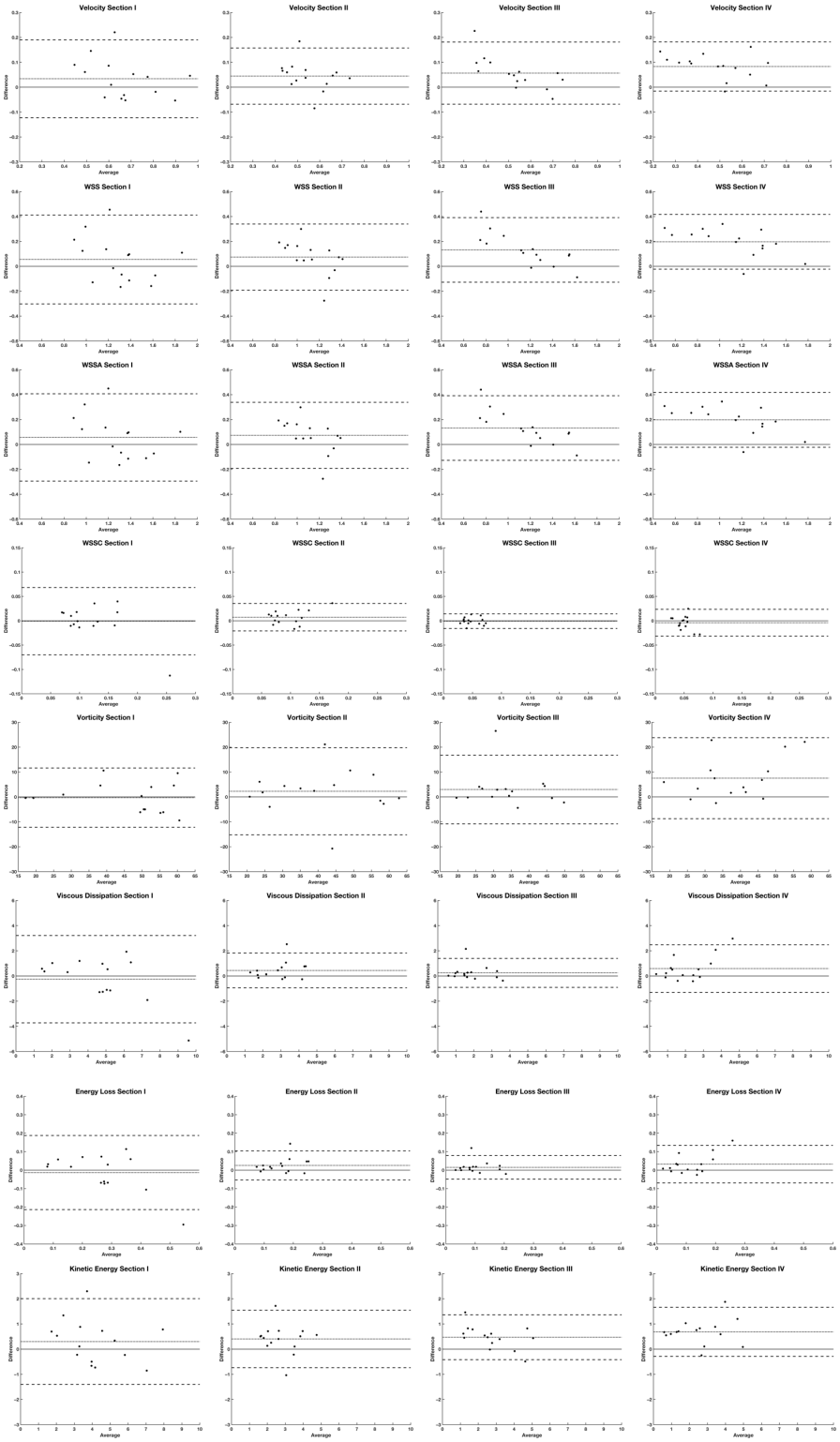

Figure A1. The Bland–Altman plots for comparing the hemodynamic parameters computed in this research, with and without self-gating: velocity; WSS; WSSA; WSSC; vorticity; viscous dissipation; energy loss; and kinetic energy. The average axis of the Bland–Altman plots corresponds to the average of the data with self-gating (SG) and without self-gating (NG), $Average = \frac{SG+NG}{2}$. The difference axis corresponds to the difference between the data with self-gating (SG) and without self-gating (NG), $Difference = SG - NG$. The difference axis shows the lines plotting the mean $\pm$ 1.96 times the standard deviation, and the zero value for comparison purposes.

Appendix B

Local Differences

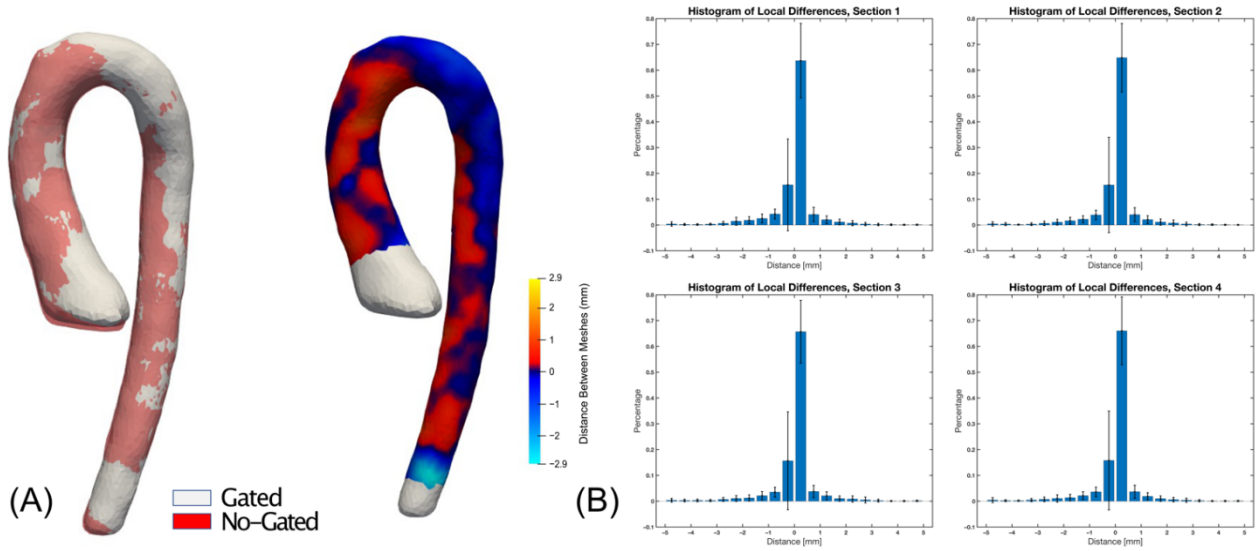

Figure A2. (**A**) The local differences of the respiratory self-gated and non-gated segmentations in a representative volunteer. The differences were calculated by measuring the Euclidean distance between each triangle of the self-gated surface mesh to the nearest triangle of the non-gated mesh along the normal direction of the first one. The region where the aorta was segmented from the left ventricle showed more significant differences between the segmentations, with and without self-gating. (**B**) A histogram of the local differences calculated at each section for all volunteers. The bar plots show the fraction of differences calculated in each section and classified by its distance in millimeters. The local differences obtained between ± 1.0 mm were 87.61% in section I, 88.27% in section II, 88.66% in section III, and 89.11% in section IV.

Table A2. The mean values of the local differences between the respiratory self-gated and non-gated segmentations, computed at each section using the signed value differences.

Hemodynamic Parameter	Section I	Section II	Section III	Section IV
Mean (mm)	−0.0811	−0.0706	−0.0505	−0.0716
Standard deviation (mm)	0.7883	0.7685	0.7548	0.7399
Minimum value (mm)	−5.1363	−4.7774	−4.7275	−4.6676
Maximum value (mm)	2.9155	2.6580	2.6624	2.9427

References

1. Dyverfeldt, P.; Ebbers, T. Comparison of respiratory motion suppression techniques for 4D flow MRI. *Magn. Reson. Med.* **2017**, *78*, 1877–1882. [CrossRef]
2. Stehning, C.; Börnert, P.; Nehrke, K.; Eggers, H.; Stuber, M. Free-breathing whole-heart coronary MRA with 3D radial SSFP and self-navigated image reconstruction. *Magn. Reson. Med.* **2005**, *54*, 476–480. [CrossRef] [PubMed]
3. Liao, J.-R.; Pauly, J.M.; Brosnan, T.J.; Pelc, N.J. Reduction of motion artifacts in cine MRI using variable-density spiral trajectories. *Magn. Reson. Med.* **1997**, *37*, 569–575. [CrossRef] [PubMed]
4. Uribe, S.; Beerbaum, P.; Sørensen, T.S.; Rasmusson, A.; Razavi, R.; Schaeffter, T. Four-dimensional (4D) flow of the whole heart and great vessels using real-time respiratory self-gating. *Magn. Reson. Med.* **2009**, *62*, 984–992. [CrossRef]
5. Henningsson, M.; Koken, P.; Stehning, C.; Razavi, R.; Prieto, C.; Botnar, R.M. Whole-heart coronary MR angiography with 2D self-navigated image reconstruction. *Magn. Reson. Med.* **2012**, *67*, 437–445. [CrossRef]
6. Weiger, M.; Börnert, P.; Proksa, R.; Schäffter, T.; Haase, A. Motion-adapted gating based onk-space weighting for reduction of respiratory motion artifacts. *Magn. Reson. Med.* **1997**, *38*, 322–333. [CrossRef] [PubMed]
7. Scott, A.D.; Keegan, J.; Firmin, D.N. High-resolution 3D coronary vessel wall imaging with near 100% respiratory efficiency using epicardial fat tracking: Reproducibility and comparison with standard methods. *J. Magn. Reson. Imaging* **2011**, *33*, 77–86. [CrossRef] [PubMed]

8. Akcakaya, M.; Gulaka, P.; Basha, T.A.; Ngo, L.H.; Manning, W.J.; Nezafat, R. Free-breathing phase contrast MRI with near 100% respiratory navigator efficiency using k-space-dependent respiratory gating. *Magn. Reson. Med.* **2014**, *71*, 2172–2179. [CrossRef] [PubMed]
9. Makowski, M.R.; Wiethoff, A.J.; Jansen, C.H.P.; Uribe, S.; Parish, V.; Schuster, A.; Botnar, R.M.; Bell, A.; Kiesewetter, C.; Razavi, R.; et al. Single breath-hold assessment of cardiac function using an accelerated 3D single breath-hold acquisition technique—Comparison of an intravascular and extravascular contrast agent. *J. Cardiovasc. Magn. Reson.* **2012**, *14*, 53. [CrossRef] [PubMed]
10. Markl, M.; Frydrychowicz, A.; Kozerke, S.; Hope, M.; Wieben, O. 4D flow MRI. *J. Magn. Reson. Imaging* **2012**, *36*, 1015–1036. [CrossRef] [PubMed]
11. Bastkowski, R.; Weiss, K.; Maintz, D.; Giese, D. Self-gated golden-angle spiral 4D flow MRI. *Magn. Reson. Med.* **2018**, *80*, 904–913. [CrossRef] [PubMed]
12. Nordmeyer, S.; Riesenkampff, E.; Crelier, G.; Khasheei, A.; Schnackenburg, B.; Berger, F.; Kuehne, T. Flow-sensitive four-dimensional cine magnetic resonance imaging for offline blood flow quantification in multiple vessels: A validation study. *J. Magn. Reson. Imaging* **2010**, *32*, 677–683. [CrossRef] [PubMed]
13. Markl, M.; Harloff, A.; Bley, T.A.; Zaitsev, M.; Jung, B.; Weigang, E.; Langer, M.; Hennig, J.; Frydrychowicz, A. Time-resolved 3D MR velocity mapping at 3T: Improved navigator-gated assessment of vascular anatomy and blood flow. *J. Magn. Reson. Imaging* **2007**, *25*, 824–831. [CrossRef] [PubMed]
14. van Ooij, P.; Semaan, E.; Schnell, S.; Giri, S.; Stankovic, Z.; Carr, J.; Barker, A.J.; Markl, M. Improved respiratory navigator gating for thoracic 4D flow MRI. *Magn. Reson. Imaging* **2015**, *33*, 992–999. [CrossRef]
15. Markl, M.; Chan, F.P.; Alley, M.T.; Wedding, K.L.; Draney, M.T.; Elkins, C.J.; Parker, D.W.; Wicker, R.; Taylor, C.A.; Herfkens, R.J.; et al. Time-resolved three-dimensional phase-contrast MRI. *J. Magn. Reson. Imaging* **2003**, *17*, 499–506. [CrossRef]
16. Montalba, C.; Urbina, J.; Sotelo, J.; Andia, M.E.; Tejos, C.; Irarrazaval, P.; Hurtado, D.E.; Valverde, I.; Uribe, S. Variability of 4D flow parameters when subjected to changes in MRI acquisition parameters using a realistic thoracic aortic phantom. *Magn. Reson. Med.* **2018**, *79*, 1882–1892. [CrossRef]
17. Sotelo, J.; Mura, J.; Hurtado, D.; Uribe, S. A Novel MATLAB Toolbox for Processing 4D Flow MRI Data. *Int. Soc. Magn. Reson. Med.* **2019**, *27*, 2.
18. Sotelo, J.; Urbina, J.; Valverde, I.; Tejos, C.; Irarrazaval, P.; Andia, M.E.; Uribe, S.; Hurtado, D.E. 3D Quantification of Wall Shear Stress and Oscillatory Shear Index Using a Finite-Element Method in 3D CINE PC-MRI Data of the Thoracic Aorta. *IEEE Trans. Med. Imaging* **2016**, *35*, 1475–1487. [CrossRef]
19. Sotelo, J.; Dux-Santoy, L.; Guala, A.; Rodríguez-Palomares, J.; Evangelista, A.; Sing-Long, C.; Urbina, J.; Mura, J.; Hurtado, D.E.; Uribe, S. 3D axial and circumferential wall shear stress from 4D flow MRI data using a finite element method and a laplacian approach. *Magn. Reson. Med.* **2018**, *79*, 2816–2823. [CrossRef]
20. Sotelo, J.; Urbina, J.; Valverde, I.; Mura, J.; Tejos, C.; Irarrazaval, P.; Andia, M.E.; Hurtado, D.E.; Uribe, S. Three-dimensional quantification of vorticity and helicity from 3D cine PC-MRI using finite-element interpolations. *Magn. Reson. Med.* **2018**, *79*, 541–553. [CrossRef] [PubMed]
21. Sotelo, J.; Valverde, I.; Martins, D.; Bonnet, D.; Boddaert, N.; Pushparajan, K.; Uribe, S.; Raimondi, F. Impact of aortic arch curvature in flow haemodynamics in patients with transposition of the great arteries after arterial switch operation. *Eur. Heart J. Cardiovasc. Imaging* **2021**, jeaa416. [CrossRef] [PubMed]
22. Arrieta, C.; Uribe, S.; Ramos-Grez, J.; Vargas, A.; Irarrazaval, P.; Parot, V.; Tejos, C. Quantitative assessments of geometric errors for rapid prototyping in medical applications. *Rapid Prototyp. J.* **2012**, *18*, 431–442. [CrossRef]